Junctional angle of a bihanded helix

Jing Yang,[1,2] Charles W. Wolgemuth,[1,3] and Greg Huber[1,4,*]

[1] *Richard Berlin Center for Cell Analysis & Modeling, University of Connecticut Health Center, Farmington, Connecticut 06030, USA*

[2] *Group of Applied Mathematics and Computational Biology, IBENS, École Normale Supérieure, Paris 75005, France*

[3] *Departments of Physics and Molecular and Cellular Biology, University of Arizona, Tucson, Arizona 85721, USA*

[4] *Kavli Institute for Theoretical Physics, University of California, Santa Barbara, California 93106, USA*

(Received 9 March 2013; revised manuscript received 11 January 2014; published 27 October 2014)

Helical filaments having sections of reversed chirality are common phenomena in the biological realm. The apparent angle between the two sections of opposite handedness provides information about the geometry and elasticity of the junctional region. In this paper, the governing differential equations for the local helical axis are developed, and asymptotic solutions of the governing equations are solved by perturbation theory. The asymptotic solutions are compared with the corresponding numerical solutions, and the relative error at second order is found to be less than 1.5% over a range of biologically relevant curvature and torsion values from 0 to 1/2 in dimensionless units.

DOI: 10.1103/PhysRevE.90.042722 PACS number(s): 87.16.Ka, 02.40.−k, 87.10.Pq, 87.16.Qp

I. INTRODUCTION

Helical shapes appear throughout the natural world but perhaps nowhere with the variety and richness as they do in biology. The helix, in both left-handed and right-handed forms, lies at the base of the molecular foundations of life on Earth, and these forms reoccur as structural motifs as one rises to higher and higher length scales on the ladder of life [1–7]. The helical structure of the DNA duplex plays an important role in genetic recombination and in the packaging of DNA in cells and viruses. Interactions between helical macromolecules are also found during the folding of proteins and the assembly of the organic matrix of bone [8]. And, at the micron scale, rotating helical flagella act as the external locomotive organelles of bacteria such as *E. coli* and *Salmonella typhimurium* and provide locomotive and structural functions within the periplasmic spaces of spirochetes such as *Treponema pallidum* [9] and *Borrelia burgdorferi* [10].

In this paper, we focus on helical filaments in which two helical conformations, identical save for opposite chirality, are seemingly concatenated (see Fig. 1). This type of conformation is reported in a number of biological systems, perhaps most famously by Darwin in his monograph *The Movements and Habits of Climbing Plants* [11]. However, the cellular and subcellular worlds are even richer in examples. The macrophage scavenger protein features a triple helix with regions of reversed chirality [12]. Bacteria such as *Bacillus subtilis* can assume helical cell-wall shapes of opposite handedness [13]. And the bacterium *Spiroplasma* swims by switching its helical body between states of right-handedness and left-handedness, with the transition between opposite chiralities propagating along the cell body as it swims [14]. Hotani [6] reported cyclic chirality transformations of *Salmonella* flagella subjected to external fluid flow while one end was tethered on glass. Conformational transitions caused by hydrodynamic torque also occur in free-swimming bacteria with multiple flagella. When a flagellar motor switches from counterclockwise to clockwise, the corresponding filament unwinds from the bundle. In the meantime, the chirality reversal initiated by motor reversal turns the left-handed helix, which had been rotated counterclockwise, into a right-handed helix rotated clockwise [15]. Hotani, in his pioneering studies [4–6], related the measured angles between reversed-chirality domains on single flagella to the angles between helices concatenated at a point.

The angle (see α in Fig. 1) between the two helical conformations, called the "block angle" by Hotani [6], can provide information about the geometry and elasticity of the transition region. In this paper, we present the results from asymptotics for the junctional angle between opposite-handed helices. Elasticity enters the problem because the curvature and torsion distributions along the filament formed by the two helices are constrained to minimize the elastic energy of the filament. The asymptotic solutions are obtained with a combination of differential geometry and perturbation theory. In cases where the detailed molecular structure of the junctional region is poorly understood, these solutions offer an opportunity to constrain the arrangement and number of molecular subunits involved.

II. FUNDAMENTAL EQUATIONS

In many biological contexts, the deformations of helical filaments (such as DNA, bacteria, and plant tendrils) are relatively small. Because the imposed curvatures are much less than the inverse diameters of the filament cross sections, the filaments respond elastically to applied forces and torques. While the theory of linear elastic filaments, which was originally developed by Kirchhoff [16], explains well the shapes of filaments with a single, preferred shape, it is less clear what shapes are possible for elastic filaments with multiple stable shapes, such as the concatenated helices previously mentioned. In order to address this question, we consider the backbone shape of a filament with multiple preferred helical forms. We define the backbone shape as a space curve, $\mathbf{r}(s)$ as a function of its arc-length parameter s, which can be completely described by a Frenet-Serret frame, in which the orthonormal triad, consisting of tangent vector $\hat{\mathbf{t}} = \dot{\mathbf{r}}$ (the dot represents the derivative with respect to s), normal vector $\hat{\mathbf{n}}$,

---

[*] huber@kitp.ucsb.edu

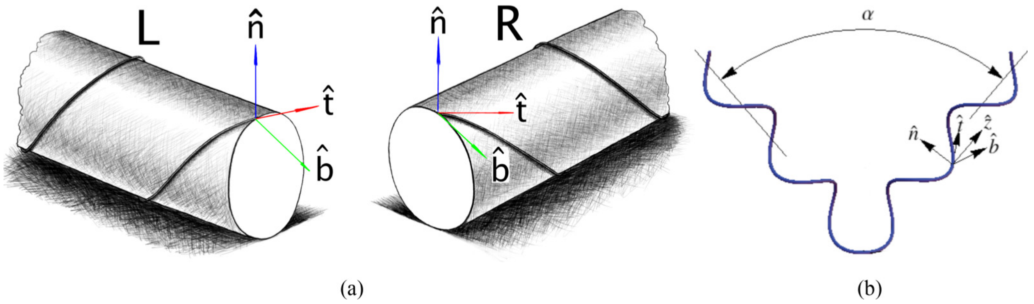

FIG. 1. (Color online) Schematic of two concatenated helices of opposite handedness, a left-handed helix (L) on the left, and a right-handed helix (R) on the right. (a) The tangent $\hat{\mathbf{t}}$, normal $\hat{\mathbf{n}}$, and binormal $\hat{\mathbf{b}}$ at the junction can be made identical; (b) connecting the two helices smoothly. Local helical axis $\hat{\mathbf{z}}$ and "block angle" α are indicated.

and binormal vector $\hat{\mathbf{b}} = \hat{\mathbf{t}} \times \hat{\mathbf{n}}$, satisfies the following matrix equation:

$$\begin{pmatrix} \dot{\hat{\mathbf{t}}} \\ \dot{\hat{\mathbf{n}}} \\ \dot{\hat{\mathbf{b}}} \end{pmatrix} = \begin{pmatrix} 0 & \kappa & 0 \\ -\kappa & 0 & \tau \\ 0 & -\tau & 0 \end{pmatrix} \begin{pmatrix} \hat{\mathbf{t}} \\ \hat{\mathbf{n}} \\ \hat{\mathbf{b}} \end{pmatrix}, \tag{1}$$

where κ is curvature and τ is torsion.

Previous work on the dynamics of bistable bacterial flagella considered filaments with a single curvature and a bistable torsion and posited an energy functional of the form [15,17,18],

$$\mathcal{E} = \int ds \left[\frac{A}{2}(\kappa - \kappa_0)^2 + g(\tau) + \frac{\gamma_\tau}{2}\left(\frac{\partial \tau}{\partial s}\right)^2 \right], \tag{2}$$

where A is the bending modulus of the filament, κ_0 is a preferred curvature, $g(\tau)$ is a quartic function that defines the two stable states for the torsion, and γ_τ defines the energetic cost for gradients in the torsion. The static solutions that minimizes this energy for an infinite filament are [15]

$$\kappa(s) = \kappa_0, \tag{3}$$

$$\tau(s) = \Delta + \Omega \tanh(s/2\xi), \tag{4}$$

where $\Delta \pm \Omega$ are the stable states of the torsion, and ξ is the front width that controls the region over which the torsion flips from one sign to the other [see Fig. 2(a)]. This front width depends on the elastic parameter γ_τ. The angle between the two helical regions is greatly affected by the aforementioned parameters, especially ξ. For long and thin filaments, the bending modulus scales as the fourth power of the radius, whereas the compressional modulus scales as the square of the radius. Therefore, it is much easier to bend a filament than to compress it. Under most forces of biological relevance, biofilaments can be treated as being inextensible.

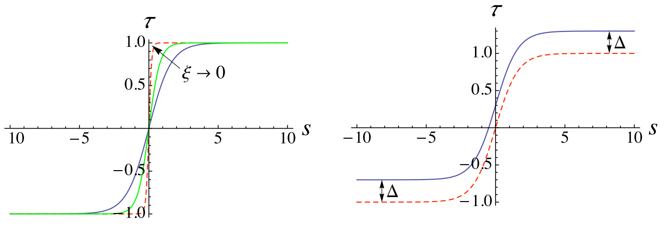

(a) Symmetric case ($\Delta = 0$) (b) Asymmetric case ($\Delta \neq 0$)

FIG. 2. (Color online) The variation of torsion τ along the backbone of the helical filament. (a) Torsion curves at different front widths ξ (0.1 for dashed red curve, 0.4 for green solid curve, 0.8 for black solid curve) if there is no shift in torsion. (b) In the asymmetric case ($\Delta \neq 0$), the torsion on the two sides of the origin is no longer antisymmetric.

Here we consider a more general energy functional that allows for bistability in the curvature and torsion. Indeed, mechanical models of the structure of bacterial flagella suggest multiple stable values for both curvature and torsion [19,20]. The simplest form of this energy is then

$$\mathcal{E} = \int ds \left[h(\kappa) + \frac{\gamma_\kappa}{2}\left(\frac{\partial \kappa}{\partial s}\right)^2 + g(\tau) + \frac{\gamma_\tau}{2}\left(\frac{\partial \tau}{\partial s}\right)^2 \right]. \tag{5}$$

In this energy, the function $h(\kappa)$ is considered to be a quartic function with two minima. The parameter γ_κ defines the energetic cost for gradients in curvature. We assume that $\gamma_\kappa \approx \gamma_\tau$ so that the length over which curvature and torsion vary is equal to ξ. As this energy is nonlinear in curvature and twist, Kirchhoff rod theory cannot be used directly to solve for the stable states. However, the elastic restoring moment can always be written as the functional derivative of the energy with respect to the strain vector [21]. Therefore, the static torque and force-free solutions for the curvature and torsion should both be hyperbolic tangent functions, analogous to what was defined above for the torsion.

Since any infinitesimal part of a space curve can be treated as part of a helix (with the same curvature and torsion as the curve at that point), the helical axis (or screw axis) is useful for describing the conformation of a filament. The local helical axis $\hat{\mathbf{z}}$ can be defined in terms of $\hat{\mathbf{t}}$ and $\hat{\mathbf{b}}$ through the following relation:

$$\hat{\mathbf{z}} = \frac{\tau \hat{\mathbf{t}}}{\sqrt{\tau^2 + \kappa^2}} + \frac{\kappa \hat{\mathbf{b}}}{\sqrt{\tau^2 + \kappa^2}}, \tag{6}$$

and the angle α between two helices can be determined by the inner product of the corresponding helical axes $\hat{\mathbf{z}}_1$ and $\hat{\mathbf{z}}_2$, i.e., $\cos(\alpha) = \hat{\mathbf{z}}_1 \cdot \hat{\mathbf{z}}_2$ (see Fig. 1). Here, for simplicity, we consider infinite length filaments. This approximation is valid as long as the transition region between handedness reversals is small compared to the total length of the filament. For bacterial flagella, this transition zone was previously estimated to be around 80 nm, which is much less than typical flagellar lengths of 1–10 μm.

In the following sections, asymptotic solutions for the block angle are explored for the cases when the front width ξ is equal to zero (Hotani case), as well as for the cases when the front width ξ is not equal to zero (finite-width case). And the finite-width cases are divided into two scenarios: one is *symmetric* in which $\Delta = 0$ and the torsion curves are antisymmetric around the origin [see Fig. 2(a)]; the other is *asymmetric* in which $\Delta \neq 0$ and the torsion curve does not possess this symmetry [see Fig. 2(b)]. Since the basic idea for the asymmetric case is essentially the same as the symmetric case, it is presented as an appendix.

III. BLOCK ANGLE

A. Hotani case ($\xi \to 0$)

In the limit where the front width ξ goes to zero, the block angle is denoted by α_0. It can be obtained from simple geometrical considerations. Considering the two helices as wrapped around separate cylinders, each helix can be represented as one of the diagonals of a rectangular "unit cell" having dimensions (pitch) × (cylinder circumference). Since the tangent vectors at the junction of the two helices have to be equal (see Fig. 3), the diagonals must be colinear, and the three (positive) angles α_0, θ_+ and $-\theta_-$ must sum to 180°: $\alpha_0 + \theta_+ + (-\theta_-) = \pi$. The angle α_0 can then be determined as $\alpha_0 = \pi - (\theta_+ - \theta_-)$, i.e.,

$$\alpha_0 = \tan^{-1}(\tau_+/\kappa_+) - \tan^{-1}(\tau_-/\kappa_-), \tag{7}$$

where $\theta_\pm$ are the pitch angles of the helices, and $\kappa_\pm$ and $\tau_\pm$ are the curvatures and torsions of the helices, respectively. In terms of the pitch P and radius R of the helices, $\kappa_\pm = R_\pm/[R_\pm^2 + (P_\pm/2\pi)^2]$ and $\tau_\pm = 2\pi P_\pm/[P_\pm^2 + (2\pi R_\pm)^2]$.

Equation (7) can also be verified via the differential geometry of space curves. For analytic simplicity, as well as to avoid singular points, a new variable is introduced as $\mathbf{Y} = \sqrt{\kappa^2 + \tau^2}\,\hat{\mathbf{z}}$ instead of using the helical axis $\hat{\mathbf{z}}$ itself. Then, $\mathbf{Y} = \tau\hat{\mathbf{t}} + \kappa\hat{\mathbf{b}}$, and the spatial evolution of $\mathbf{Y}$ is given by

$$\dot{\mathbf{Y}} = \dot{\tau}\hat{\mathbf{t}} + \dot{\kappa}\hat{\mathbf{b}}. \tag{8}$$

Substituting Eq. (3) and (4) into Eq. (8), and integrating on both sides, the solution of the ordinary differential equation (8) can be obtained as

$$\mathbf{Y} = \int_0^s \frac{d\tau(u)}{du}\hat{\mathbf{t}}\,du + \kappa_0\,\hat{\mathbf{b}}(0). \tag{9}$$

It can be determined from Eq. (4) that $\lim_{\xi\to 0} d\tau(u)/du = \Omega\delta(u)$. Thus, the limiting values of $\mathbf{Y}$ at $+\infty$ and $-\infty$ are

$$\begin{aligned}\lim_{s\to+\infty}\mathbf{Y} &= \mathbf{Y}_+ = \sqrt{\kappa_0^2 + \Omega_+^2}\,\hat{\mathbf{z}}_+ = \kappa_0\hat{\mathbf{b}}(0) + \Omega_+\hat{\mathbf{t}}(0),\\ \lim_{s\to-\infty}\mathbf{Y} &= \mathbf{Y}_- = \sqrt{\kappa_0^2 + \Omega_-^2}\,\hat{\mathbf{z}}_- = \kappa_0\hat{\mathbf{b}}(0) + \Omega_-\hat{\mathbf{t}}(0),\end{aligned} \tag{10}$$

where $\Omega_+ = \Omega + \Delta, \hat{\mathbf{z}}_+$, and $\Omega_- = -\Omega + \Delta, \hat{\mathbf{z}}_-$ are the torsions and helical axes at $+\infty$ and $-\infty$, respectively. Therefore, $\cos(\alpha_0) = \mathbf{z}_+ \cdot \mathbf{z}_- = (\kappa_0^2 + \Omega_+\Omega_-)/(\sqrt{\kappa_0^2 + \Omega_+^2}\sqrt{\kappa_0^2 + \Omega_-^2})$, and the block angle can be determined as

$$\alpha_0 = \tan^{-1}(\Omega_+/\kappa_0) - \tan^{-1}(\Omega_-/\kappa_0), \tag{11}$$

consistent with the result obtained from geometrical reasoning.

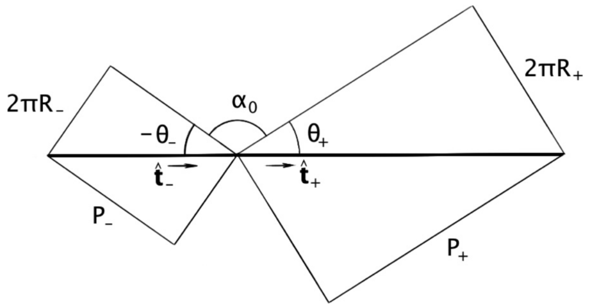

FIG. 3. The geometrical explanation of the angle α_0 (adapted from Ref. [15]). $R_\pm$ are the radii of the helices, and $P_\pm$ are the pitches of the helices.

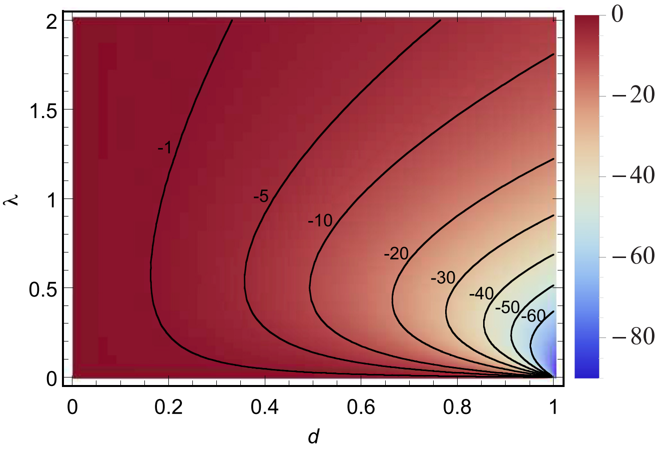

FIG. 4. (Color online) The variation of block angle before and after shifting as a function of shift ratio d and torsion-curvature ratio λ. The isolines are the variation $\tilde{\alpha}_0 - \alpha_0$ in degrees.

For the Hotani case, the asymmetric shift Δ of the torsion curve can greatly affect the block angle; the variation after shifting can be up to 60° (see Fig. 4) according to Eq. (11). If the block angle after shifting is denoted as $\tilde{\alpha}_0$, the variation of the angle before and after can be written as

$$\tilde{\alpha}_0 - \alpha_0 = -\tan^{-1}\frac{2d^2\lambda}{d^2(\lambda^2 - 1) + (\lambda^2 + 1)^2}, \tag{12}$$

where $d = \Delta/\Omega$, and $\lambda = \kappa_0/\Omega$. Fig. 4 shows the block-angle variation as a function of shift ratio d and curvature-torsion ratio λ, where the contour lines are the block-angle variation isolines labeled in degrees. One can see that the variation of the angle is typically less than 10° when the shift is no more than 50%. The variation in the angle increases with the shift, but decreases with increasing curvature-torsion ratio.

However, when the front width ξ is not equal to zero, both block angles α_0 and $\tilde{\alpha}_0$ are affected. This will be discussed next in a section devoted to the finite-width case.

B. Finite-width case ($\xi \neq 0$)

For the finite-width case (when $\xi \neq 0$), both the torsion τ and the helical axis $\hat{\mathbf{z}}$ are changing along the filament, and the problem is complicated by the front width ξ, as well as by the shift of the torsion curve Δ. The evolution of the helical axis along the filament has to be solved from its governing equations, along with the boundary conditions. The block

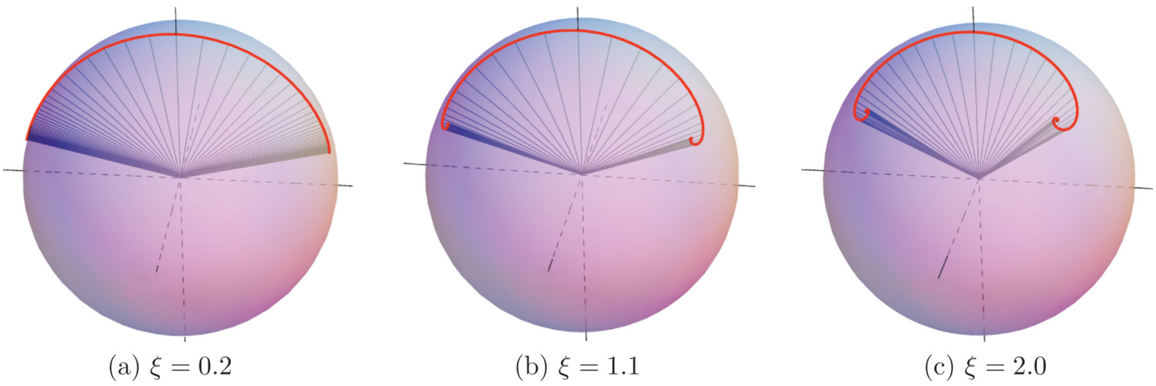

FIG. 5. (Color online) The evolution of the helical axis $\hat{\mathbf{z}}$ on a sphere at different front widths.

angle can then be determined from the inner product of the helical axes at $+\infty$ and $-\infty$.

For the *symmetric case*, the governing equation for the helical axis is derived from the Frenet-Serret formulas as the following ordinary differential equation (in which the helical axis $\hat{\mathbf{z}}$ is incorporated implicitly into the variable $\mathbf{Y}$):

$$\begin{aligned}&\mathbf{Y}''' + 4\tanh(\eta)\mathbf{Y}'' + [(2+\mathrm{K}^2) + (2+\mathrm{T}^2)\tanh^2(\eta)]\mathbf{Y}'\\&\quad -\mathrm{T}^2\tanh(\eta)\mathrm{sech}^2(\eta)\mathbf{Y} = \mathbf{0}.\end{aligned} \tag{13}$$

Here curvature, torsion, and arc length are nondimensionalized by the front width ξ as $\mathrm{K} = 2\xi\kappa_0$, $\mathrm{T} = 2\xi\Omega$, and $\eta = s/2\xi$, respectively, and the prime represents the derivative with respect to η. The corresponding boundary conditions for the above differential equation are

$$\mathbf{Y}(0) = \begin{pmatrix}0\\0\\\mathrm{K}\end{pmatrix}, \quad \mathbf{Y}'(0) = \begin{pmatrix}\mathrm{T}\\0\\0\end{pmatrix}, \quad \mathbf{Y}''(0) = \begin{pmatrix}0\\\mathrm{TK}\\0\end{pmatrix}.$$

The details of the derivation of Eq. (13) and its boundary conditions are presented in Appendix B. Similarly, for the *asymmetric case*, the governing equation for the helical axis can be written as

$$\begin{aligned}&\mathbf{Y}''' + 4\tanh(\eta)\mathbf{Y}''\\&\quad +[(2+\mathrm{K}^2+\mathrm{D}^2) + 2\mathrm{TD}\tanh(\eta) + (2+\mathrm{T}^2)\tanh^2(\eta)]\mathbf{Y}'\\&\quad -\mathrm{sech}^2(\eta)[\mathrm{TD} + \mathrm{T}^2\tanh(\eta)]\mathbf{Y} = \mathbf{0},\end{aligned} \tag{14}$$

where $\mathrm{D} = 2\xi\Delta$. The corresponding boundary conditions are

$$\mathbf{Y}(0) = \begin{pmatrix}\mathrm{D}\\0\\\mathrm{K}\end{pmatrix}, \quad \mathbf{Y}'(0) = \begin{pmatrix}\mathrm{T}\\0\\0\end{pmatrix}, \quad \mathbf{Y}''(0) = \begin{pmatrix}0\\\mathrm{TK}\\0\end{pmatrix},$$

where the three-vectors are represented by the three components in the x, y, and z directions. It is difficult to solve Eqs. (13) and (14) analytically, but their asymptotic solutions can be obtained through perturbation theory.

C. Helical-axis trajectory

An interesting phenomenon that should be mentioned here is that the trajectory swept out by the helical axis lies on the surface of a sphere. If all the bases of the local helical axis $\hat{\mathbf{z}}$ along the filament are translated to the center of a unit sphere, the heads of the helical axes trace out a continuous trajectory on the surface of the unit sphere (see Fig. 5). The length of the trajectory can be determined as

$$\begin{aligned}\int_{-\infty}^{+\infty} |\dot{\hat{\mathbf{z}}}|\, ds &= \int_{\Omega_-}^{\Omega_+} \frac{\kappa_0\, d\tau}{\kappa_0^2 + \tau^2}\\&= \tan^{-1}(\Omega_+/\kappa_0) - \tan^{-1}(\Omega_-/\kappa_0),\end{aligned} \tag{15}$$

which is identical to the block angle for the Hotani case ($\xi = 0$). It can be seen from Eq. (15) that the total length of the trajectory is constant for fixed κ_0 and Ω, but the shape of the trajectory, as well as the actual block angle, changes as a function of front width ξ. The trajectory is distorted into a curly shape on the spherical surface at large ξ and becomes more and more "straight" as ξ decreases, eventually becoming a geodesic on the unit sphere in the limit $\xi \to 0$ (see Fig. 5). The block angle is the angle between the two helical axes at the opposite ends of the trajectory; thus, the block angles for the finite-width cases are always less than their counterparts for the Hotani cases α_0.

IV. PERTURBATION METHODS

Perturbation methods [22] can be used to find approximate solutions to problems which cannot be solved exactly. For the *symmetric case*, two perturbation variables ϵ_1 and ϵ_2 are introduced into Eq. (13) to solve the third-order differential equation, i.e.,

$$\begin{aligned}&\mathbf{Y}''' + 4\tanh(\eta)\mathbf{Y}'' + [(2+\epsilon_2) + (2+\epsilon_1)\tanh^2(\eta)]\mathbf{Y}'\\&\quad -\epsilon_1\tanh(\eta)\mathrm{sech}^2(\eta)\mathbf{Y} = \mathbf{0},\end{aligned} \tag{16}$$

and a double series expansion

$$\mathbf{Y} = \sum_{i,j=0}^{\infty} \epsilon_2^i \epsilon_1^j \mathbf{Y}_{ij} \tag{17}$$

is proposed as the solution of the differential equation (13). After substituting the double series expansion into Eq. (16), collecting coefficients of like powers of $\epsilon_2^i\epsilon_1^j$, and letting the coefficients equal to zero, we get a new series of third-order differential equations for $\mathbf{Y}_{ij}$ of the following form:

$$\mathbf{Y}_{ij}''' + 4\tanh(\eta)\mathbf{Y}_{ij}'' + 2[1+\tanh^2(\eta)]\mathbf{Y}_{ij}' = \mathbf{NH}_{ij}, \tag{18}$$

where the indices $i,j = 0,1,2,\ldots,$ and the $\mathbf{NH}_{ij}$ are the nonhomogeneous terms of the new series of differential

TABLE I. Nonhomogeneous terms $\mathbf{NH}_{ij}$ in the differential equations (18).

i	j	$\mathbf{NH}_{ij}$
0	0	$\mathbf{0}$
0	1	$\mathrm{sech}^2(\eta)\tanh(\eta)\mathbf{Y}_{00} - \tanh^2(\eta)\mathbf{Y}'_{00}$
1	0	$-\mathbf{Y}'_{00}$
1	1	$\mathrm{sech}^2(\eta)\tanh(\eta)\mathbf{Y}_{10} - \mathbf{Y}'_{01} - \tanh^2(\eta)\mathbf{Y}'_{10}$
0	2	$\mathrm{sech}^2(\eta)\tanh(\eta)\mathbf{Y}_{01} - \tanh^2(\eta)\mathbf{Y}'_{01}$
2	0	$-\mathbf{Y}'_{10}$
…		

equations; their specific expressions are listed in Table I. The corresponding boundary conditions for these new differential equations are

$$\mathbf{Y}_{00}(0) = \begin{pmatrix} 0 \\ 0 \\ \mathrm{K} \end{pmatrix}, \quad \mathbf{Y}'_{00}(0) = \begin{pmatrix} \mathrm{T} \\ 0 \\ 0 \end{pmatrix}, \quad \mathbf{Y}''_{00}(0) = \begin{pmatrix} 0 \\ \mathrm{KT} \\ 0 \end{pmatrix}, \quad \text{and}$$

$$\mathbf{Y}_{ij}(0) = \mathbf{Y}'_{ij}(0) = \mathbf{Y}''_{ij}(0) = \begin{pmatrix} 0 \\ 0 \\ 0 \end{pmatrix} \quad (\text{for } i,\ j \neq 0).$$

Similarly, for the *asymmetric case*, three perturbation variables ε_1, ε_2, and ε_3 are introduced into Eq. (14) as

$$\begin{aligned} &\mathbf{Y}''' + 4\tanh(\eta)\mathbf{Y}'' \\ &\quad + [(2+\varepsilon_2) + 2\varepsilon_3\tanh(\eta) + (2+\varepsilon_1)\tanh^2(\eta)]\mathbf{Y}' \\ &\quad - [\varepsilon_3 + \varepsilon_1\tanh(\eta)]\mathrm{sech}^2(\eta)\mathbf{Y} = \mathbf{0}, \end{aligned} \tag{19}$$

and a triple series expansion is assumed as the solution of the differential equation (19), i.e.,

$$\mathbf{Y} = \sum_{i,j,k=0}^{\infty} \varepsilon_3^i \varepsilon_2^j \varepsilon_1^k \mathbf{Y}_{ijk}. \tag{20}$$

Then the new series of differential equations for $\mathbf{Y}_{ijk}$ becomes

$$\mathbf{Y}'''_{ijk} + 4\tanh(\eta)\mathbf{Y}''_{ijk} + 2[1+\tanh^2(\eta)]\mathbf{Y}'_{ijk} = \mathbf{NH}_{ijk}, \tag{21}$$

in which $\mathbf{NH}_{ijk}$ are nonhomogeneous terms that are listed in Table V. The corresponding boundary conditions are

$$\mathbf{Y}_{000}(0) = \begin{pmatrix} 0 \\ 0 \\ \mathrm{K} \end{pmatrix}, \quad \mathbf{Y}'_{000}(0) = \begin{pmatrix} \mathrm{T} \\ 0 \\ 0 \end{pmatrix},$$

$$\mathbf{Y}''_{000}(0) = \begin{pmatrix} 0 \\ \mathrm{KT} \\ 0 \end{pmatrix},$$

$$\text{and} \quad \mathbf{Y}_{ijk}(0) = \mathbf{Y}'_{ijk}(0) = \mathbf{Y}''_{ijk}(0) = \begin{pmatrix} 0 \\ 0 \\ 0 \end{pmatrix} \quad (\text{for } i,\ j,\ k \neq 0).$$

After the differential equations (18) and (21) are solved iteratively, the solutions $\mathbf{Y}_{ij}$ and $\mathbf{Y}_{ijk}$ are substituted into Eqs. (17) and (20), respectively, and setting $\epsilon_1 = \mathrm{T}^2$ and $\epsilon_2 = \mathrm{K}^2$ for the *symmetric case*, and $\varepsilon_1 = \mathrm{T}^2$, $\varepsilon_2 = \mathrm{K}^2 + \mathrm{D}^2$, and $\varepsilon_3 = \mathrm{TD}$ for the *asymmetric case*, then the asymptotic solutions for Eqs. (13) and (14) are obtained as infinite series.

V. RESULTS AND DISCUSSION

The asymptotic solutions of the differential equations (18) and (21) for the finite-width cases are obtained with

TABLE II. Solutions $\mathbf{Y}_{ij}$ of the differential equations (18).[a]

i	j	Components	$\mathbf{Y}_{ij}$
0	0	x	$\mathrm{T}\tanh(\eta)$
		y	$\mathrm{KT}q(\eta)$
		z	K
0	1	x	0
		y	$-\mathrm{KT}\big\{\tanh(\eta)\int_0^\eta \log^3[\cosh(x)]\mathrm{csch}^2(x)\,dx\big\}/6$
		z	$\mathrm{K}\big\{\tanh(\eta)\int_0^\eta \log^2[\cosh(x)]\mathrm{csch}^2(x)\,dx\big\}/2$
1	0	x	$-\mathrm{T}\big[\int_0^\eta x^2\mathrm{sech}^2(x)\,dx\big]/2$
		y	$-\mathrm{KT}\big[\int_0^\eta x^3\mathrm{sech}^2(x)\,dx\big]/6$
		z	0
1	1	x	$\mathrm{T}\big\{q(\eta)\int_0^\eta f(x)\,dx + \int_0^\eta \log[\cosh(x)]f(x)\,dx - \tanh(\eta)\int_0^\eta xf(x)\,dx\big\}$
		y	$\mathrm{KT}\big\{q(\eta)\int_0^\eta g(x)\,dx + \int_0^\eta \log[\cosh(x)]g(x)\,dx - \tanh(\eta)\int_0^\eta xg(x)\,dx\big\}$
		z	$\mathrm{K}\big\{q(\eta)\int_0^\eta h(x)\,dx + \int_0^\eta \log[\cosh(x)]h(x)\,dx - \tanh(\eta)\int_0^\eta xh(x)\,dx\big\}$
0	2	x	0
		y	$\mathrm{KT}\big\{5\tanh(\eta)\int_0^\eta \log^4[\cosh(x)]\,dx - \log^5[\cosh(\eta)]\big\}/120$
		z	$\mathrm{K}\big\{\log^4[\cosh(\eta)] - 4\tanh(\eta)\int_0^\eta \log^3[\cosh(x)]\,dx\big\}/24$
2	0	x	$\mathrm{T}\big(\eta^3\{\eta\tanh(\eta) - 4\log[\cosh(\eta)]\} + 12\int_0^\eta x^2\log[\cosh(x)]\,dx\big)/24$
		y	$\mathrm{KT}\big(\eta^4\{\eta\tanh(\eta) - 5\log[\cosh(\eta)]\} + 20\int_0^\eta x^3\log[\cosh(x)]\,dx\big)/120$
		z	0
…			

[a] $f(x) = \tanh(x)\int_0^x u\tanh(u)\,du$
$g(x) = \{\tanh(x)\int_0^x u^2\tanh(u)\,du + \int_0^x \log^2[\cosh(u)]\,du\}/2$
$h(x) = -\int_0^x \log[\cosh(u)]\,du$, and $q(\eta) = \eta\tanh(\eta) - \log[\cosh(\eta)]$

TABLE III. The limits of $\mathbf{Y}_{ij}$ when $\eta \to +\infty$.

i	j	Components	$\lim_{\eta\to+\infty} \mathbf{Y}_{ij}$
0	0	x	T
		y	$\mathrm{KT}\log 2$
		z	K
0	1	x	0
		y	$\mathrm{KT}[\pi^2\log 2 - 4\log^3 2 - 6\zeta(3)]/24$
		z	$\mathrm{K}[\pi^2 - 12\log^2 2]/24$
1	0	x	$-\mathrm{T}\pi^2/24$
		y	$-3\zeta(3)\mathrm{KT}/16$
		z	0
1	1	x	$\mathrm{T}\pi^4/1440$
		y	$0.063\,823\,2\mathrm{KT}$
		z	$\mathrm{K}[90\zeta(3)\log 2 - \pi^4]/480$
0	2	x	0
		y	$0.016\,045\,3\mathrm{KT}$
		z	$\mathrm{K}\{80[\log^4 2 + 6\zeta(3)\log 2] - 3\pi^4 - 40\pi^2\log^2 2\}/1920$
2	0	x	$7\pi^4\mathrm{T}/5760$
		y	$15\zeta(5)\mathrm{KT}/256$
		z	0
...			

perturbation methods, and the block angle is determined from the asymptotic solutions. For convenience, the block angles for these cases are compared with the Hotani angle, and the difference is denoted the block-angle correction $\Delta\alpha$. The expressions for the angular corrections, as well as their numerical magnitudes, are discussed for both *symmetric* and *asymmetric cases*. Only the symmetric case is treated in this section; the asymmetric case is presented as Appendix A for the interested reader.

The nonhomogeneous terms $\mathbf{NH}_{ij}$ for the differential equations (18) are listed in Table I, and the solutions $\mathbf{Y}_{ij}$ for the series of ordinary differential equations (18) are listed in Table II. For the sake of simplicity, only the solutions of second order or less are listed.

When $\eta \to +\infty$ or $-\infty$, the asymptotic solutions $\mathbf{Y} = \sum_{i,j=0}^{\infty}\mathrm{K}^{2i}\mathrm{T}^{2j}\mathbf{Y}_{ij}$ converge to vectors $\mathbf{Y}_+$ or $\mathbf{Y}_-$, respectively, for example,

$$\mathbf{Y}_+ = \lim_{\eta\to+\infty}\mathbf{Y} = \sum_{i,j=0}^{\infty}\mathrm{K}^{2i}\mathrm{T}^{2j}\big(\lim_{\eta\to+\infty}\mathbf{Y}_{ij}\big). \tag{22}$$

The limits of $\mathbf{Y}_{ij}$ at $+\infty$ are listed in Table III, and $\mathbf{Y}_-$ can be obtained from $\mathbf{Y}_+$ according to the following equation:

$$\mathbf{Y}_- = \begin{pmatrix} -1 & 0 & 0 \\ 0 & 1 & 0 \\ 0 & 0 & 1 \end{pmatrix}\mathbf{Y}_+.$$

The block angle is determined from the inner product of the helical axes $\hat{\mathbf{z}}$ at $+\infty$ and $-\infty$ as

$$\cos(\alpha) = \hat{\mathbf{z}}(+\infty)\cdot\hat{\mathbf{z}}(-\infty) = \frac{\mathbf{Y}_+\cdot\mathbf{Y}_-}{\mathrm{K}^2+\mathrm{T}^2} = \frac{\mathrm{K}^2-\mathrm{T}^2+\mathcal{S}}{\mathrm{K}^2+\mathrm{T}^2}, \tag{23}$$

where $\mathcal{S} = \sum_{i,j=1}^{\infty}\mathrm{C}_{ij}\mathrm{K}^{2i}\mathrm{T}^{2j}$ (coefficients C_{ij} are listed in Table IV). The dot product $\cos(\alpha)$ can also be expanded as a Taylor series around α_0, the block angle for the Hotani case [see Eq. (7) or (11)]: $\cos(\alpha) = \cos(\alpha_0) - \sin(\alpha_0)\Delta\alpha - \cos(\alpha_0)(\Delta\alpha)^2/2 + \cdots$, where $\Delta\alpha = \alpha - \alpha_0$ is the angular correction that we are seeking.

Now, the expressions for $\cos(\alpha_0)$ and $\sin(\alpha_0)$ corresponding to the Hotani case are easily obtained:

$$\cos(\alpha_0) = (\mathrm{K}^2-\mathrm{T}^2)/(\mathrm{K}^2+\mathrm{T}^2), \tag{24}$$

$$\sin(\alpha_0) = 2\mathrm{KT}/(\mathrm{K}^2+\mathrm{T}^2). \tag{25}$$

After substituting the Taylor series for $\cos(\alpha)$ into Eq. (23) and truncating terms higher than second order in the Taylor series, we get the following quadratic equation for $\Delta\alpha$:

$$-\frac{\mathrm{K}^2-\mathrm{T}^2}{2}(\Delta\alpha)^2 - 2\mathrm{KT}\Delta\alpha = \mathcal{S}. \tag{26}$$

TABLE IV. Coefficients C_{ij} in the variable $\mathcal{S}$

i	j	C_{ij}
1	1	$\pi^2/6$
1	2	$-\pi^4/360$
1	3	$0.015\,969\,5$
1	4	$-0.001\,183\,79$
1	5	$0.000\,257\,451$
2	1	$-\pi^4/120$
2	2	$0.160\,131$
2	3	$-0.017\,778\,5$
2	4	$0.002\,048\,12$
3	1	$\{7\pi^6 + 810[3\zeta^2(3) + 10\log(2)\zeta(5)]\}/69\,120$
3	2	$-0.051\,227\,7$
3	3	$0.006\,023\,14$
4	1	$-49\pi^8/33\,177\,600 - 45\zeta(3)\zeta(5)/2048$
4	2	$0.007\,755\,47$
5	1	$225\zeta^2(5)/65\,536$
...		

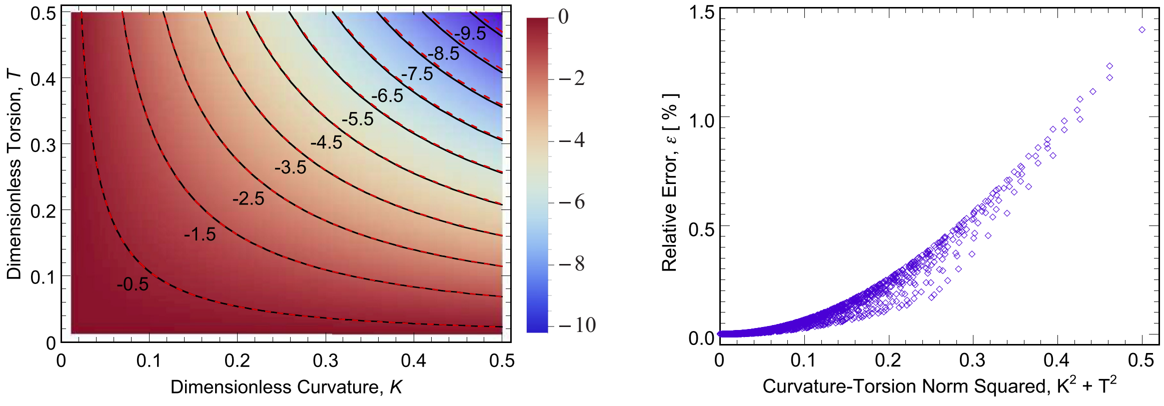

(a) (b)

FIG. 6. (Color online) Block-angle correction as a function of K and T, including the quadratic term in the Taylor series for $\cos\alpha$. (a) Contour plot of block-angle correction labeled in degrees. (b) Relative errors between numerical and perturbation results.

Therefore, the block-angle correction $\Delta\alpha$ can be solved as

$$\Delta\alpha = \begin{cases} -\mathcal{S}/2\mathrm{KT} & \text{if } \mathrm{K} = \mathrm{T} \\ \frac{-2\mathrm{KT}+\sqrt{4\mathrm{K}^2\mathrm{T}^2-2\mathcal{S}(\mathrm{K}^2-\mathrm{T}^2)}}{\mathrm{K}^2-\mathrm{T}^2} & \text{if } \mathrm{K} \neq \mathrm{T} \end{cases}. \qquad (27)$$

Actually, the second part (when K≠T) of Eq. (27) is just a correction to the first part (when K = T), since the square-root term in the second part can be asymptotically expanded as follows:

$$\begin{aligned} &\sqrt{4\mathrm{K}^2\mathrm{T}^2 - 2\mathcal{S}(\mathrm{K}^2-\mathrm{T}^2)} \\ &= 2\mathrm{KT}\sqrt{1 - \frac{\mathcal{S}(\mathrm{K}^2-\mathrm{T}^2)}{2\mathrm{K}^2\mathrm{T}^2}} \\ &= 2\mathrm{KT}\left[1 - \frac{\mathcal{S}(\mathrm{K}^2-\mathrm{T}^2)}{4\mathrm{K}^2\mathrm{T}^2} - \frac{\mathcal{S}^2(\mathrm{K}^2-\mathrm{T}^2)^2}{32\mathrm{K}^4\mathrm{T}^4} + \cdots\right] \\ &= 2\mathrm{KT} - \frac{\mathcal{S}(\mathrm{K}^2-\mathrm{T}^2)}{2\mathrm{KT}} - \frac{\mathcal{S}^2(\mathrm{K}^2-\mathrm{T}^2)^2}{16\mathrm{K}^3\mathrm{T}^3} + \cdots . \end{aligned}$$

Then the second part of Eq. (27) turns out to be

$$\begin{aligned} &\frac{-2\mathrm{KT} + \sqrt{4\mathrm{K}^2\mathrm{T}^2 - 2\mathcal{S}(\mathrm{K}^2-\mathrm{T}^2)}}{\mathrm{K}^2-\mathrm{T}^2} \\ &= -\frac{\mathcal{S}}{2\mathrm{KT}} - \frac{\mathcal{S}^2}{16}\frac{\mathrm{K}^2-\mathrm{T}^2}{\mathrm{K}^3\mathrm{T}^3} + \cdots , \end{aligned}$$

which has the form of a correction to the $K = T$ case.

The block-angle correction as a function of K and T is shown in Fig. 6(a), in which the contour lines are correction isolines labeled in degrees [the dash lines are the results from Eq. (27) and the solid lines are the numerical results obtained by solving the Frenet-Serret equations (1) with appropriate initial conditions]. The angular corrections $\Delta\alpha$ increase with both K and T, and the contour lines are almost symmetric with respect to the line K = T (there is slight difference when K and T are exchanged). Since the exchange of K and T is equivalent to switching the binormal vector $\hat{\mathbf{b}}$ and the tangent vector $\hat{\mathbf{t}}$, and it does not greatly affect $\hat{\mathbf{z}}$ [according to Eq. (6)].

Figure 6(b) shows the relative error ε between the asymptotic solution [Eq. (27)] from perturbation theory and the

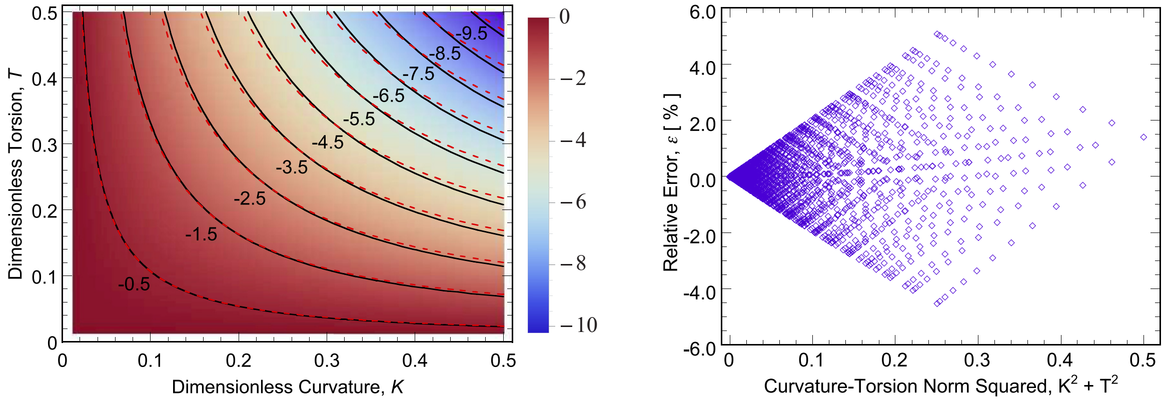

(a) (b)

FIG. 7. (Color online) Block-angle correction as a function of K and T (without quadratic analysis). (a) Contour plot of block-angle correction labeled in degrees. (b) Relative errors between numerical and perturbation results.

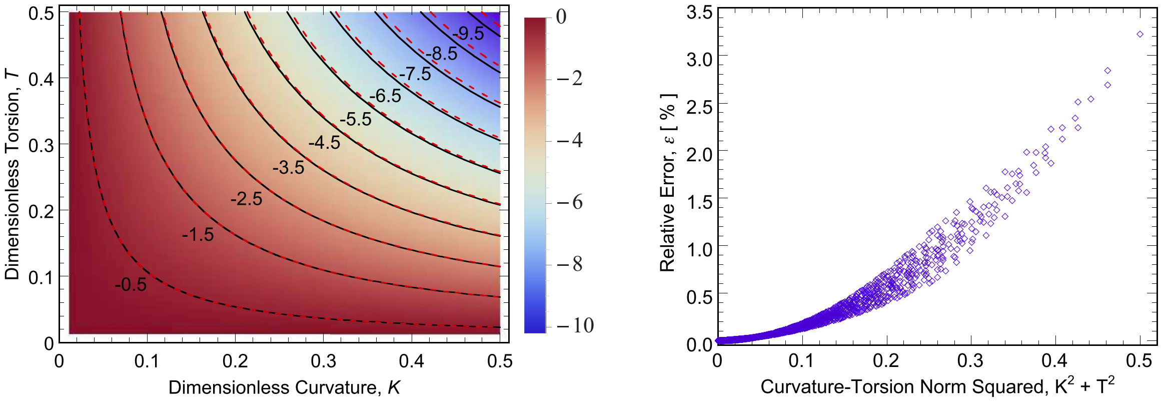

(a)

(b)

FIG. 8. (Color online) Truncated form of block-angle correction [see Eq. (28)] as a function of K and T. (a) Contour plot of block-angle correction labeled in degrees. (b) Relative errors between the numerical and perturbation results.

numerical solution, i.e.,

$$(\Delta\alpha_{\text{num}} - \Delta\alpha_{\text{per}})/\Delta\alpha_{\text{num}} \times 100\%\,,$$

as a function of the square of the curvature-torsion norm $K^2 + T^2$. The relative error increases monotonically with $K^2 + T^2$, and when $K^2 + T^2$ is 0.5, the relative error is only about 1.5%.

The inclusion of the quadratic term of the Taylor series expansion for $\cos(\alpha)$ in solving for $\Delta\alpha$ greatly improves the accuracy of the estimation of angular correction. For comparison, Fig. 7(a) shows the numerical results and the asymptotic solutions without the quadratic term included [see Eq. (26)]. The solid lines are the results from numerical solution, and the dashed lines are the results from asymptotics. The difference between the numerics and asymptotics increases with the dimensionless curvature K and torsion T [relative errors are shown in Fig. 7(b) as a function of $K^2 + T^2$], and the relative error is much higher compared to that in the quadratic analysis. The relative error can reach 5%, when $K^2 + T^2$ is around 0.25, and seems to increase linearly with $K^2 + T^2$. (The decrease after 0.25 is just due to lack of data.)

For convenience, the first three terms in Eq. (27) (after the expression for $\mathcal{S}$ is substituted in) can be taken as an approximation of Eq. (27) by truncating the remaining terms for small KT, i.e.,

$$\Delta\alpha \sim -\frac{\pi^2}{12}KT + \frac{\pi^4}{320}KT^3 + \frac{7\pi^4}{2880}K^3T, \tag{28}$$

and the results from the truncated form Eq. (28) are shown in Fig. 8(a). The truncated form agrees well with the numerical results at small K and T, and the relative errors are shown in Fig. 8(b) as a function of $K^2 + T^2$. Relative error increases with $K^2 + T^2$, and the relative error is generally less than 1% when $K^2 + T^2$ is less than 0.25.

Many bacterial flagella are built from a helical arrangement of 11 protofilaments comprised of the single protein flagellin [23]. The flagellin monomer is bistable and can be in either a long or short state [24]. This bistability of the flagellin monomer leads to polymorphism of the flagellum: a single flagellum has multiple stable helical states. During bacterial swimming, rotation of the flagella can cause the flagellum to flip between these stable states, and purified and reconstituted flagella are sometimes seen where part of the flagellum is in one state and another part of the flagellum is in a different helical state. In the context of elasticity, there should be an energetic cost for having a transition between two different states on the same flagellum. The analysis presented here allows a means for estimating the elastic parameters that define the energetic costs for gradients in curvature and torsion. For example, Hotani reconstituted bacterial flagella using mixtures of wild-type and mutant flagellin [3,5]. He then measured discrepancies in the block angle of the filament that were on order of 1–4 degrees. Based on these deviations in block angle, we predict that the front width ξ is between 32 and 64 nm for bacterial flagella, and the corresponding dimensionless variables K and T are less than 0.4, with D less than 0.2, suggesting that the results presented in this paper are relevant to this system. Hotani's measurements also suggest that larger curvature or torsion discrepancies produce larger deviations in the block angle. Therefore, we expect that ξ is dependent on the strain between neighboring flagellin monomers in the flagellum.

VI. CONCLUSION

An asymptotic solution for the angle between two helical conformations of a filament of reversed chirality is presented. The filament's shape is determined by minimizing a quartic strain energy, leading to a scaled version of the exact governing equations for the local helical-axis orientation. These equations are tackled with a combination of perturbation theory and differential geometry. The junctional region between the two handednesses possesses a characteristic length scale, the front width ξ, and the cases of zero and finite ξ are both considered. The finite-ξ cases are further subdivided into two cases depending on the symmetry properties of the filament's torsion around the junction. The correction to the angle gives information about the finite transition region, and comparing the asymptotic solution with numerics gives relative errors of less than 1.5% for values of the (dimensionless) curvature-torsion norm squared $K^2 + T^2$ up to 0.5. The solutions obtained provide a means for estimating elastic parameters for polymorphic biofilaments; for example, we discuss how our solutions relate to Hotani's experimental data on bacterial flagella [3,5]. Reconciling the classical elasticity theory of bihanded filaments, and similar biomorphological problems,

TABLE V. Nonhomogeneous terms $\mathbf{NH}_{ijk}$ in the differential equations (21).

i	j	k	$\mathbf{NH}_{ijk}$
0	0	0	$\mathbf{0}$
1	0	0	$\mathrm{sech}^2(\eta)\mathbf{Y}_{000} - 2\tanh(\eta)\mathbf{Y}'_{000}$
0	1	0	$-\mathbf{Y}'_{000}$
0	0	1	$\mathrm{sech}^2(\eta)\tanh(\eta)\mathbf{Y}_{000} - \tanh^2(\eta)\mathbf{Y}'_{000}$
…			

with detailed models of their underlying subunit geometry is an area for future work.

ACKNOWLEDGMENTS

This research was partially supported by the National Science Foundation under NSF grant PHY11-25915 (KITP, G.H.). Support from the Richard Berlin Center for Cell Analysis & Modeling is also gratefully acknowledged.

APPENDIX A: ASYMMETRIC CASE

The nonhomogeneous terms in the differential equations (21) are listed in Table V, and the solutions $\mathbf{Y}_{ijk}$ are listed in Table VI (only the solutions second order or less are listed). The limits of $\mathbf{Y}_{ijk}$ when η tends to $-\infty$ or $+\infty$ are listed in Table VII.

The asymptotic solution $\mathbf{Y}$ of the differential equation (21) can be written as an infinite series, i.e., $\mathbf{Y} = \sum_{i,j,k=0}^{\infty}(\mathrm{TD})^i(\mathrm{K}^2+\mathrm{D}^2)^j\mathrm{T}^{2k}\mathbf{Y}_{ijk}$, and the limits of $\mathbf{Y}$ at $+\infty$ or $-\infty$ are

$$\mathbf{Y}_{+} = \lim_{\eta\to+\infty}\mathbf{Y} = \sum_{i,j,k=0}^{\infty}(\mathrm{TD})^i(\mathrm{K}^2+\mathrm{D}^2)^j\mathrm{T}^{2k}\Big(\lim_{\eta\to+\infty}\mathbf{Y}_{ijk}\Big) \tag{A1}$$

$$\mathbf{Y}_{-} = \lim_{\eta\to-\infty}\mathbf{Y} = \sum_{i,j,k=0}^{\infty}(\mathrm{TD})^i(\mathrm{K}^2+\mathrm{D}^2)^j\mathrm{T}^{2k}\Big(\lim_{\eta\to-\infty}\mathbf{Y}_{ijk}\Big) \tag{A2}$$

As before, the angle α can be determined from

$$\cos(\alpha) = \mathbf{z}_{+}\cdot\mathbf{z}_{-} = \frac{\mathbf{Y}_{+}\cdot\mathbf{Y}_{-}}{\sqrt{(\mathrm{K}^2+\mathrm{T}_{+}^2)(\mathrm{K}^2+\mathrm{T}_{-}^2)}},$$

where $\mathrm{T}_{+} = \mathrm{T}+\mathrm{D}$ and $\mathrm{T}_{-} = -\mathrm{T}+\mathrm{D}$. As in the *symmetric case*, $\cos(\alpha)$ can be expanded in a Taylor series around $\tilde{\alpha}_0$, i.e.,

$$\cos(\alpha) = \cos(\tilde{\alpha}_0) - \sin(\tilde{\alpha}_0)\Delta\alpha - \frac{\cos(\tilde{\alpha}_0)}{2}(\Delta\alpha)^2 + \cdots, \tag{A3}$$

where

$$\cos(\tilde{\alpha}_0) = \frac{\mathrm{D}^2+\mathrm{K}^2-\mathrm{T}^2}{\sqrt{(\mathrm{K}^2+\mathrm{T}_{+}^2)(\mathrm{K}^2+\mathrm{T}_{-}^2)}},$$

$$\sin(\tilde{\alpha}_0) = \frac{2\mathrm{KT}}{\sqrt{(\mathrm{K}^2+\mathrm{T}_{+}^2)(\mathrm{K}^2+\mathrm{T}_{-}^2)}},$$

and $\Delta\alpha = \alpha - \tilde{\alpha}_0$. $\Delta\alpha$ can be approximated from the above quadratic equation (A3) after truncating terms higher than second order:

$$\Delta\alpha = \frac{-2\mathrm{KT} + \sqrt{4\mathrm{K}^2\mathrm{T}^2 - 2\mathcal{A}(\mathrm{D}^2+\mathrm{K}^2-\mathrm{T}^2)}}{\mathrm{D}^2+\mathrm{K}^2-\mathrm{T}^2}, \tag{A4}$$

where $\mathcal{A} = \mathbf{Y}_{+}\cdot\mathbf{Y}_{-} - (\mathrm{D}^2+\mathrm{K}^2-\mathrm{T}^2) = \sum_{i,j=1,k=0}^{\infty} B_{ijk}\mathrm{K}^{2i}\mathrm{T}^{2j}\mathrm{D}^{2k}$ (the coefficients B_{ijk} are listed in Table VIII).

Figure 9 presents the block-angle correction as a function of curvature and torsion when the torsion curves are shifted from the symmetric position. The contour lines are the angular correction isolines labeled in degrees [the dashed lines are the results from Eq. (A4), and the solid lines are the results from numerical solutions of the Frenet-Serret equations with appropriate boundary conditions].

The shift Δ should not be larger than the torsion Ω, otherwise the filament cannot have reversed chirality. The percentage shift of the torsion curve (Δ/Ω) is therefore employed to investigate how shifting affects the block angle. It can be seen in Fig. 9 that the shift of the torsion curve does

TABLE VI. Solutions $\mathbf{Y}_{ijk}$ of the differential equations (21).

i	j	k	Components	$\mathbf{Y}_{ijk}$
0	0	0	x	$\mathrm{D}+\mathrm{T}\tanh(\eta)$
			y	$\mathrm{KT}\{\eta\tanh(\eta) - \log[\cosh(\eta)]\}$
			z	K
1	0	0	x	$\mathrm{T}\big\{\log^2[\cosh(\eta)] - 2\tanh(\eta)\int_0^\eta \log[\cosh(x)]\,dx\big\}/2 + \mathrm{D}\big[\int_0^\eta x^2\mathrm{sech}^2(x)\,dx\big]/2$
			y	$\mathrm{KT}\big\{\eta\log^2[\cosh(\eta)] - 2\tanh(\eta)\int_0^\eta x\log[\cosh(x)]\,dx - \int_0^\eta \log^2[\cosh(x)]\,dx\big\}/2$
			z	$\mathrm{K}\big\{\eta^2\tanh(\eta) - 2\eta\log[\cosh(\eta)] + 2\int_0^\eta \log[\cosh(x)]\,dx\big\}/2$
0	1	0	x	$\mathrm{T}\big\{2\eta\log[\cosh(\eta)] - \eta^2\tanh(\eta) - 2\int_0^\eta \log[\cosh(x)]\,dx\big\}/2$
			y	$\mathrm{KT}\big\{3\eta^2\log[\cosh(\eta)] - \eta^3\tanh(\eta) - 6\int_0^\eta x\log[\cosh(x)]\,dx\big\}/6$
			z	0
0	0	1	x	$\mathrm{D}\big\{2\tanh(\eta)\int_0^\eta \log[\cosh(x)]\,dx - \log^2[\cosh(\eta)]\big\}/2$
			y	$\mathrm{KT}\big\{\log^3[\cosh(\eta)] - 3\tanh(\eta)\int_0^\eta \log^2[\cosh(x)]\,dx\big\}/6$
			z	$\mathrm{K}\big\{2\tanh(\eta)\int_0^\eta \log[\cosh(x)]\,dx - \log^2[\cosh(\eta)]\big\}/2$
.	.	.		

TABLE VII. The limits of $\mathbf{Y}_{ijk}$ when $\eta \to +\infty$ or $-\infty$.

i	j	k	Components	$\lim_{\eta\to+\infty} \mathbf{Y}_{ijk}$	$\lim_{\eta\to-\infty} \mathbf{Y}_{ijk}$
0	0	0	x	$\mathrm{D}+\mathrm{T}$	$\mathrm{D}-\mathrm{T}$
			y	$\mathrm{KT}\log 2$	$\mathrm{KT}\log 2$
			z	K	K
1	0	0	x	$[12\mathrm{T}\log^2 2+(\mathrm{D}-\mathrm{T})\pi^2]/24$	$[12\mathrm{T}\log^2 2-(\mathrm{T}+\mathrm{D})\pi^2]/24$
			y	$\mathrm{KT}[2\pi^2\log 2-21\zeta(3)]/48$	$\mathrm{KT}[21\zeta(3)-2\pi^2\log 2]/48$
			z	$\mathrm{K}\pi^2/24$	$-\mathrm{K}\pi^2/24$
0	1	0	x	$-\pi^2\mathrm{T}/24$	$\pi^2\mathrm{T}/24$
			y	$-3\zeta(3)\mathrm{KT}/16$	$-3\zeta(3)\mathrm{KT}/16$
			z	0	0
0	0	1	x	$\mathrm{D}[\pi^2-12\log^2 2]/24$	$\mathrm{D}[\pi^2-12\log^2 2]/24$
			y	$\mathrm{KT}[\pi^2\log 2-6\zeta(3)-4\log^3 2]/24$	$\mathrm{KT}[\pi^2\log 2-6\zeta(3)-4\log^3 2]/24$
			z	$\mathrm{K}[\pi^2-12\log^2 2]/24$	$\mathrm{K}[\pi^2-12\log^2 2]/24$
.	.	.			

not affect significantly the block-angle correction, there being only slight variation when the percentage shift is even 90%. However, the error of the asymptotic solution increases with the percentage shift.

APPENDIX B: DERIVATION OF THE GOVERNING EQUATION FOR THE HELICAL AXIS

According to the Frenet-Serret formulas [see Eq. (1)], $\dot{\hat{\mathbf{t}}} = \kappa\,\hat{\mathbf{n}}$, and hence

$$\ddot{\hat{\mathbf{t}}} = \kappa_0 \dot{\hat{\mathbf{n}}} \tag{B1}$$

if the curvature κ is a constant κ_0 [the case considered in this paper; see Eq. (3)]. For the same reason, we can obtain $\dot{\mathbf{Y}} = \dot{\tau}\hat{\mathbf{t}}$ from Eq. (8), i.e.,

$$\hat{\mathbf{t}} = \frac{\dot{\mathbf{Y}}}{\dot{\tau}}. \tag{B2}$$

Similarly, after taking a derivative on both sides of Eq. (6), we obtain

$$\dot{\hat{\mathbf{z}}} = \frac{\kappa\dot{\tau}-\dot{\kappa}\tau}{(\kappa^2+\tau^2)^{3/2}}(\kappa\hat{\mathbf{t}}-\tau\hat{\mathbf{b}}) = \frac{\dot{\kappa}\tau-\kappa\dot{\tau}}{(\kappa^2+\tau^2)^{3/2}}\dot{\hat{\mathbf{n}}}.$$

Then, after substituting $\hat{\mathbf{z}} = \mathbf{Y}/\sqrt{\kappa^2+\tau^2}$ and $\kappa = \kappa_0$ into the above equation and rearranging, we obtain

$$\dot{\hat{\mathbf{n}}} = -\frac{\left(\kappa_0^2+\tau^2\right)^{3/2}}{\kappa_0\dot{\tau}}\frac{d}{ds}\left(\frac{\mathbf{Y}}{\sqrt{\kappa_0^2+\tau^2}}\right). \tag{B3}$$

Substituting Eqs. (B2) and (B3) into Eq. (B1), we then obtain

$$\frac{d^2}{ds^2}\left(\frac{\dot{\mathbf{Y}}}{\dot{\tau}}\right) + \frac{\left(\kappa_0^2+\tau^2\right)^{3/2}}{\dot{\tau}}\frac{d}{ds}\left(\frac{\mathbf{Y}}{\sqrt{\kappa_0+\tau^2}}\right) = \mathbf{0}.$$

After substituting Eq. (4) into the above equation, rearranging and dedimensionalizing, we get the governing equation for the helical axis, i.e., Eq. (13).

The corresponding boundary conditions can be obtained from $\mathbf{Y} = \tau\,\hat{\mathbf{t}} + \kappa\,\hat{\mathbf{b}}$ and its first and second derivatives by setting $s = 0$, $\hat{\mathbf{t}}(0) = (1, 0, 0)^{\mathrm{T}}$, $\hat{\mathbf{n}}(0) = (0, 1, 0)^{\mathrm{T}}$, and $\hat{\mathbf{b}}(0) = (0, 0, 1)^{\mathrm{T}}$.

TABLE VIII. Coefficients B_{ijk} in the variable $\mathcal{A}$.

i	j	k	B_{ijk}
1	1	0	$\pi^2/6$
1	1	1	$-[\pi^4+216\zeta(3)\log 2]/576$
1	1	2	$9\zeta^2(3)/256$
1	2	0	$\{\pi^4+24\pi^2\log^2 2-48[\log^4 2+6\zeta(3)\log 2]\}/576$
1	2	1	$[-4\pi^4\log^2 2+48\log 2(\pi^2+3\log^2 2)\zeta(3)-225\zeta^2(3)]/2304$
1	3	0	$[\pi^2\log 2-4\log^3 2-6\zeta(3)]^2/576$
2	1	0	$-[\pi^4+216\zeta(3)\log 2]/576$
2	1	1	$9\zeta^2(3)/128$
2	2	0	$\zeta(3)[-\pi^2\log 2+4\log^3 2+6\zeta(3)]/64$
3	1	0	$9\zeta^2(3)/256$
. . .			

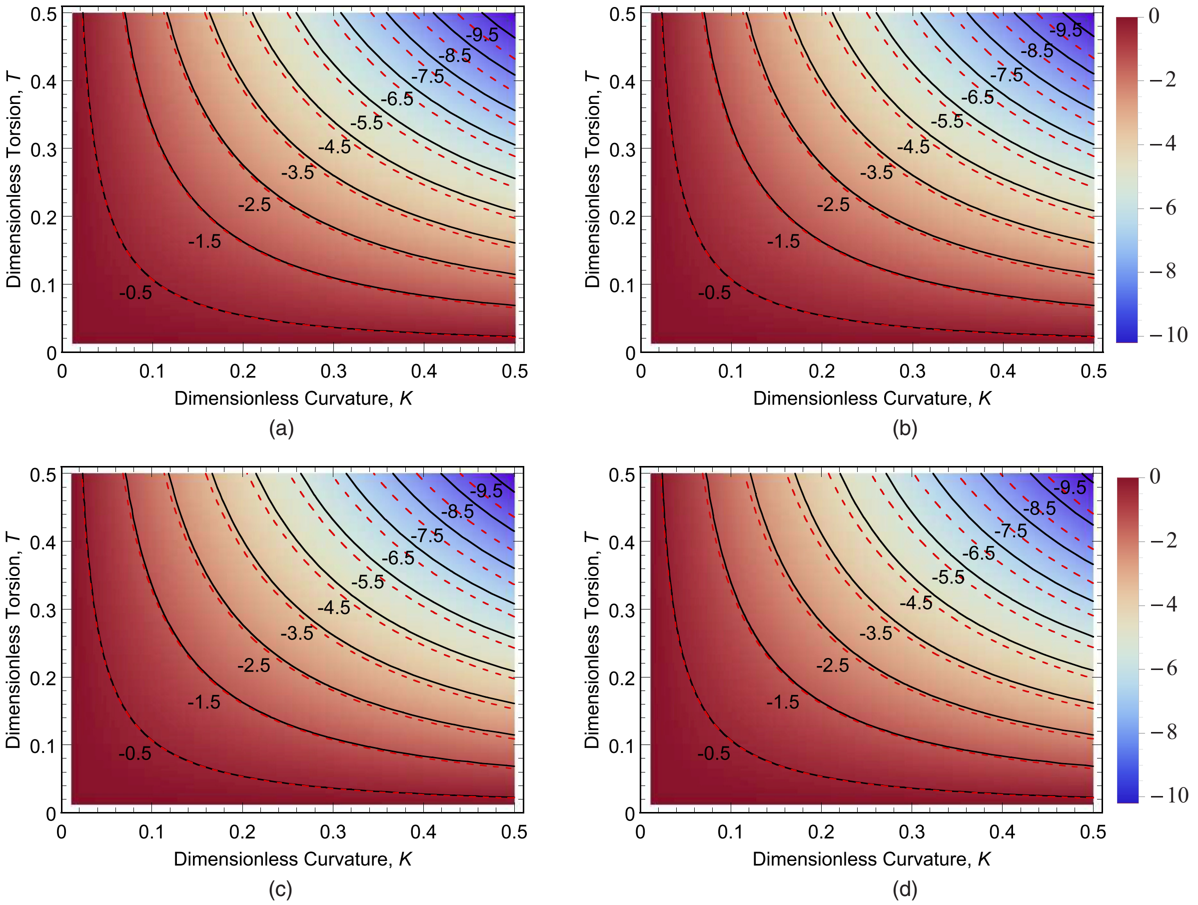

(a) (b) (c) (d)

FIG. 9. (Color online) The $\Delta\alpha$ isolines represented in degrees as a function of dimensionless curvature and torsion for different percentages (a) 1%, (b) 30%, (c) 60%, (d) 90% of torsion shift Δ/Ω.

---

[1] S. Trachtenberg and I. Hammel, J. Struct. Biol. **109**, 18 (1992).
[2] M. Gardner, *The Ambidextrous Universe* (Allen Lane, Penguin, London, 1967).
[3] H. Hotani, J. Mol. Biol. **106**, 151 (1976).
[4] H. Hotani, J. Mol. Biol. **129**, 305 (1979).
[5] H. Hotani, Biosystems **12**, 325 (1980).
[6] H. Hotani, J. Mol. Biol. **156**, 791 (1982).
[7] K. S. Cheon, J. V. Selinger, and M. M. Green, Angew. Chem., Int. Ed. Engl. **39**, 1482 (2000).
[8] A. A. Kornyshev, D. J. Lee, S. Leikin, and A. Wynveen, Rev. Mod. Phys. **79**, 943 (2007).
[9] C. Dombrowski, W. Kan, M. A. Motaleb, N. W. Charon, R. E. Goldstein, and C. W. Wolgemuth, Biophys. J. **96**, 4409 (2009).
[10] J. Yang, G. Huber, and C. W. Wolgemuth, Phys. Rev. Lett. **107**, 268101 (2011).
[11] C. Darwin, *The Movements and Habits of Climbing Plants* (John Murray, London, 1888).
[12] J. W. Galloway, *Biological Asymmetry and Handedness* (Wiley-Interscience, New York, 1991).
[13] M. J. Tilby, Nature (London) **266**, 450 (1977).
[14] J. Yang, C. W. Wolgemuth, and G. Huber, Phys. Rev. Lett. **102**, 218102 (2009).
[15] R. E. Goldstein, A. Goriely, G. Huber, and C. W. Wolgemuth, Phys. Rev. Lett. **84**, 1631 (2000).
[16] G. Kirchhoff, *Vorlesungen über Mathematische Physik* (B. G. Teubner, Leipzig, 1883).
[17] C. W. Wolgemuth, Ph.D. thesis, University of Arizona, 2000.
[18] D. Coombs, G. Huber, J. O. Kessler, and R. E. Goldstein, Phys. Rev. Lett. **89**, 118102 (2002).
[19] S. V. Srigiriraju and T. R. Powers, Phys. Rev. Lett. **94**, 248101 (2005).
[20] S. V. Srigiriraju and T. R. Powers, Phys. Rev. E **73**, 011902 (2006).
[21] W. Kan and C. W. Wolgemuth, Biophys. J. **93**, 54 (2007).
[22] C. M. Bender and S. A. Orszag, *Advanced Mathematical Methods for Scientists and Engineers* (McGraw-Hill, New York, 1978).
[23] C. R. Calladine, Nature (London) **255**, 121 (1975).
[24] C. R. Calladine, J. Mol. Biol. **118**, 457 (1978).